Article:
Ren, K., Hu, J., Bi, C. et al. (6 more authors) (2024) Strongly-Confined CsPbI3 Quantum Dots by Surface Cleaning-Induced Ligand Exchange for Spectrally Stable Pure-Red Light-Emitting Diodes with Efficiency Exceeding 26%. ACS Materials Letters, 6. pp. 4115-4123. ISSN 2639-4979

https://doi.org/10.1021/acsmaterialslett.4c00912

Strongly-Confined $CsPbI_3$ Quantum Dots by Surface Cleaning-Induced Ligand Exchange for Spectrally Stable Pure-Red Light-Emitting Diodes with Efficiency Exceeding 26%

Ke Ren[1,2†], Jingcong Hu[4†], Chenghao Bi[1,2,3†*], Shibo Wei[1,2], Xingyu Wang[5,6], Nora H. de Leeuw[5,6], Yue Lu[4*], Manling Sui[4*], Wenxin Wang[1,2*]

[1] Qingdao Innovation and Development Base, Harbin Engineering University, Qingdao 266000, P. R. China.

[2] College of Physics and Optoelectronic Engineering, Harbin Engineering University, Harbin 150001, P. R. China.

[3] Yantai Research Institute, Harbin Engineering University, Yantai 264000, P.R. China.

[4] Beijing Key Lab of Microstructure and Property of Advanced Materials, College of Materials Science and Engineering, Beijing University of Technology, Beijing 100124, P. R. China.

[5] School of Chemistry, University of Leeds, Leeds LS2 9JT, UK.

[6] Department of Earth Sciences, Utrecht University, 3584 CB Utrecht, The Netherlands.

E-mail: chenghao.bi@hrbeu.edu.cn; luyue@bjut.edu.cn; mlsui@bjut.edu.cn; wenxin.wang@hrbeu.edu.cn

Abstract

The advancement of pure-red perovskite light-emitting diodes (PeLEDs) is still a challenge because of surface "wastes" (like surface vacancies and excessive insulating ligands) on quantum dots (QDs). Herein, we develop a method to synthesize single-halide pure-red $CsPbI_3$ QDs, combining strong quantum confinement effect and meticulous surface-cleaning induced ligand exchange. We achieve pure-red emitting QDs by controlling the size and uniformity under iodide-rich conditions. Subsequently, vacancy defects and insulating ligands are cleared through introducing acid. Then this surface-cleaning process induces ligand exchange to further inhibit the non-radiative recombination and improve electrical property of QDs. These QDs show a pure-red photoluminescence (PL) at 635 nm with the PL quantum yield (PLQY) of 99%. Finally, PeLEDs, which utilize these QDs, demonstrate a pure-red electroluminescence (EL) peak at 638 nm with a maximum external quantum efficiency (EQE) of 26.0% and an excellent half-lifetime (T_{50}) of 490 min at an original luminance of 102 cd/m^2.

Table of Contents Image

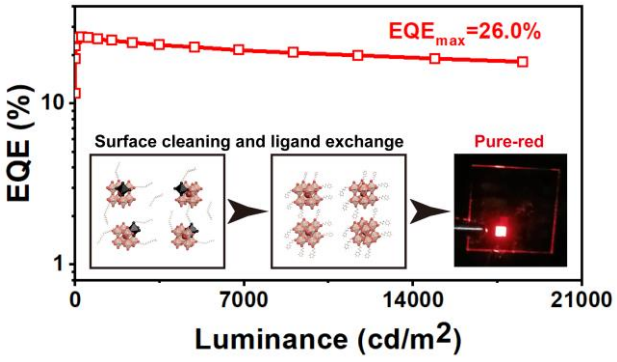

Lead halide perovskite quantum dots (QDs) are viewed as favorable successors for high-definition display applications[1-6], by strengths of the remarkable photoluminescence quantum yield (PLQY)[7-9], excellent defect tolerance[10,11], and narrow emission line-width[12,13], among other benefits. The unique emission characteristics of perovskite QDs help to generate a concentrated energy spectrum, resulting in narrow-band emission of the primary color triplets (red, green, blue) with high brightness and color purity[14-16]. Perovskite QDs light-emitting diodes (PeLEDs) have earned concern in recently[17]. Because excellent performance improvement has shown tremendous strides. Two of these improvements are very pleasing, including extremely high external quantum efficiency (EQE), and a very wide range of emission colors with ultra-high luminance[2,18]. In order to fast replace conventional display applications and use perovskite QDs in high-definition, the balanced development of red, green, and blue QDs is very important[19-21]. Because these three colors are the basis for the blending of other colors. Owing to the continuing and extensive research on the composition and surface engineering of QDs, the development of green PeLEDs has made considerable progress. The EQE has already reached 28.9%, which meets the requirements of commercial applications[22]. But it is still difficult to make bright, high-efficiency PeLEDs with a peak of pure-red electroluminescence (EL) at around 635 nm, because red QDs are susceptible to phase changes and phase separation, resulting in the deterioration of their optoelectronic properties[23].

In principle, perovskite QDs composed of Br/I mixed halides can be considered as widely deployed candidates to achieve pure-red emission. However, serious halide segregation causes broadening and a displacement of the EL peak in the PeLEDs[24]. Generally speaking, intrinsic halide vacancies in mixed-halide QDs can act as ion migration sites, allowing Br and I ions to reorganize and create localized areas that are rich in Br and I ions[25]. This surface defect problem is not insurmountable. Rationally designed surface ligand engineering is an effective way to passivate surface defects in QDs. A new method to treat the $CsPb(Br/I)_3$ QDs utilizing mixed ligands of 1-dodecanethiol and tetrabutylammonium iodide is reported in a recent study[26]. The high-efficiency PeLED emitting at 636 nm has a supreme luminance (2653 cd/m^2), and a peak EQE of 21.8%. However, the spectral stability of this device is not ideal. The highest EQE of this device is measured at a luminance of less than 50 cd/m^2. In addition, oleic acid (OA) and oleylamine (OAm) on mixed halide perovskite QDs are easily removed, forming a large number of defects[27]. The effects of these issues of perovskite QDs require an in-depth investigation. Recently, it has been shown that nano-sized single-halide $CsPbI_3$ QDs (~ 5 nm) with strong quantum confinement effects can achieve pure-red emission and effectively avoid the drawbacks caused by mixed halides[28]. However, there is still much space for improvement in the functioning of PeLEDs based on these QDs, due to the existence of "wastes" (such as surface defects and excessive insulating ligands). Unlike the large-sized perovskite nanocrystals, strongly-confined $CsPbI_3$ QDs may maintain an unstable state for two reasons. Firstly, the surface-area-to-volume ratio of these QDs is high. Secondly, plenty of surface defects are caused by the disappearance of weakly bound ligands from the QDs surface. This may eventually lead to the decomposition of QDs. Because iodide defects can

induce agglomeration and phase change of $CsPbI_3$ QDs[29,30]. Furthermore, the existence of long-chain ligands on the QD surface is unfavorable for charge transport. Consequently, this leads to a reduction in the luminance of the device[31]. This emphasizes the need for improved ligand modulations to achieve pure-red PeLEDs in real-world applications. Finally, the exciton binding energy (E_B) for a strongly confined system is generally high, resulting in severe Auger recombination[32], which could cause an accumulation of charges in PeLEDs, leading to the roll-off of EQE.

Here, a type of high-performance pure-red PeLEDs via strongly-confined single-halide $CsPbI_3$ QDs is reported. Initially, QDs, whose size is about 5 nm, are synthesized under iodide-rich conditions, which can efficiently control the nucleus and growth process of QDs. Subsequently, we introduce a strategy of surface cleaning and ligand exchange to remove "wastes" on the surface of the QDs. Acid is employed to clean the octahedra with defects on the QDs surface, and creates binding sites for ligand exchange between short-chain 3-phenyl-1-propylamine (3-PA) and initial long-chain ligands, engendering the extremely low occurrence of defects and high carrier mobility. Calculations based on the Density Functional Theory (DFT) have demonstrated that the 3-PA exhibits stronger binding to the QDs, which can effectively passivate surface vacancies and act as efficient electron acceptors to attract and store excess charge carriers in QDs. Hence, the accumulation of carriers is alleviated and the E_B of the QDs is minimized. And Auger recombination of the QDs is changed to a direction of decreasing. The optimized QDs exhibit a pure-red peak at around 635 nm, whose full-width-at-half-maximum (FWHM) is 31 nm. And the PLQY of these QDs is 99%. The PeLEDs display a pure-red electroluminescent (EL) peak emitting at precisely 638 nm. This EL peak can be precisely quantified in terms of Commission Internationale de l'Illumination (CIE) coordinates, which is determined to be (0.701, 0.297). Our devices have a peak EQE as high as 26.0%. These devices show a slow efficiency roll-off, and the top luminance is 18500 cd/m^2. Under an original luminance of 102 cd/m^2, the long operational half-life (T_{50}) of these devices is 490 min.

In general, mixed-halides $CsPbBr_xI_{3-x}$ QDs synthesized by hot-injection method[26] are used to achieve pure-red emission (**Figure 1a**), called QDs-M. Nevertheless, a great deal of halide vacancies is left on the outside of QDs-M, after the surface halide anions and the long-chain ligands are lost, deteriorating the PLQY and stability[33]. In addition, ultrafast growth dynamics of QDs-M result in a poor size distribution[7,34], whereas halide ion diffusion in the QDs-M will accelerate phase separation and eventually form Br-rich and I-rich QDs with different emissions[35]. Therefore, we have designed pure-red QDs based on single-halide and strongly-confined confinement (SQDs) with a consistent variety of diameter distribution and an average size of only ~ 5 nm. The growth dynamics of SQDs are controlled by plenty of iodide sources in the synthetic technique. This process efficiently avoids the disadvantages caused by mixed halides. However, there are usually a large number of incomplete octahedra and free organic ligands presenting on the perovskite QDs surface, which are called "wastes". The electrical and optical characteristics of SQDs are severely affected by these "wastes". Commonly surface ligands are easily stripped off under external stimuli[36], leading to the low PLQY and agglomeration of SQDs. Subsequently, we introduce a hydrobromic

acidic solution (HBr) to clean the surface wastes of SQDs (SQDs cleaned by HBr are called SQDs-H), which efficiently removes surface defects and excessive insulating ligands. However, this process can also leave undercoordinated sites on the SQDs surface, which will lead to poor stability, such as phase change and degradation, of SQDs-H. Hence, we have used these sites to induce subsequent ligand exchange. Short-chain benzene ring ligands are added to passivate the surface defects, improving the conductivity and stability of SQDs. Finally, we have obtained pure-red emitting SQDs with excellent properties, and named as SQDs-T. SQDs-T are treated by surface-cleaning and ligand exchange.

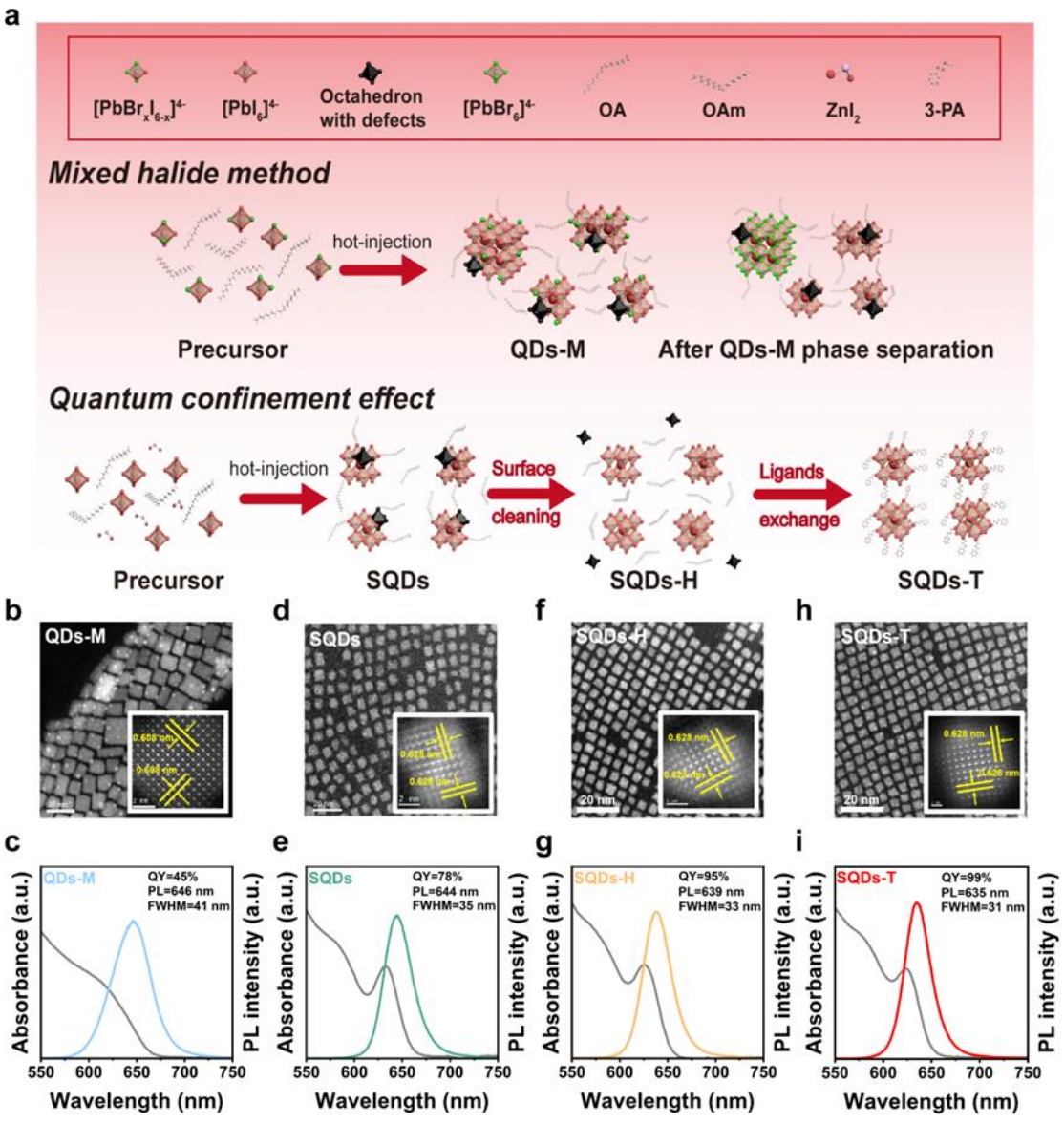

Figure 1. A description of fabrication and optical properties of QDs. (a) Schematic depicting the process of ligand exchange caused by surface-cleaning; Transmission electron microscopy (TEM) and high-resolution transmission electron microscopy (HRTEM) images of (b) QDs-M, (d) SQDs, (f) SQDs-H, and (h) SQDs-T; UV-vis absorption (grey line) as well as photoluminescence (PL) spectra (color line) of (c) QDs-M, SQDs, (g) SQDs-H, and (i) SQDs-T.

We have synthesized a series of QDs with red emission according to the above

design based on the traditional hot-injection method. TEM images are obtained to analyze the shape and size of different QDs. UV-visible absorption and PL spectrums are utilized to probe their optical characteristics. There is little uniformity in the size distribution of QDs-M which is 9.6 ± 3.3 nm and the lattice spacing of it is measured to be 0.608 nm (**Figure 1b, Figures S1a** and **S2a**). Additionally, the FWHM of 41 nm and lower PLQY are demonstrated by these QDs, which display a maximum intensity of emission at 646 nm. (**Figure 1c**). In contrast, SQDs show a more homogeneous size distribution of 4.6 ± 0.9 nm (**Figure 1d** and **Figure S1b**). In **Figure 1e**, the SQDs exhibit a sharper absorption peak compared to QDs-M cause of the stronger quantum confinement and narrower size distribution. They exhibit a pure-red emission, which has a PL emission at 644 nm. The FWHM of SQDs (35 nm) is narrower, compared with QDs-M. The PLQY increases to 78%. All of them indicate that the performance of SQDs is slightly better than QDs-M because of the relatively reduced trap density. This appearance can be attributed to the optimized nucleation and growth process in an iodide-rich environment. We compare the in-situ PL spectra of the growing process and the UV-vis spectra of Pb-precursor solutions of QDs-M and SQDs. QDs-M and SQDs have various quantities of halide, so we use these differences in observations to further illustrate the growth mechanism of SQDs (**Figures S3** and **S4**). These measurements indicate the formation of $[PbI_6]^{4-}$ octahedra in the iodine-rich ion environment. This ultimately leads to a fast nucleation and growth speed of QDs. The Ostwald ripening process is effectively inhibited. In order to provide the Ostwald ripening process in SQDs is suppressed, we compare the optical and morphological properties of QDs-M and SQDs produced at different quenching speeds (**Figure S5**). Thereby the final perovskite QDs achieve a narrow size-distribution[37]. Although the growth dynamics improves the quality of SDQs compared to QDs-M, there are still a large number of defects on the surface, especially the naked vacancy defects (**Figure 1d**). After the surface cleaning process by HBr solution, SQDs-H show a smaller average size with a more uniform size distribution of (4.4 ± 0.5 nm) and a clearer boundary (**Figure 1f** and **Figure S1c**). During the surface cleaning process, incomplete octahedra and excessive long-chain ligands are taken out, which causes the size reduction of the SQDs-H. The SQDs-H also exhibit a slight blue-shifted trend, mainly in the form of excitonic absorption peak and PL emission peak (639 nm) with a narrow FWHM of 33 nm (**Figure 1g**). These are appertaining to the smaller size and more consistent shape distribution of SQDs-H, which is confirmed by TEM results. Also, the blue-shift of spectra also arises from the reduced surface defects due to the peeling of incomplete octahedrons during the surface cleaning rather than the incorporation of Br^- (**Figure S6**). In addition, the significantly improved PLQY of SQDs-H (95%) indicates the efficient removal of halide vacancies during the surface-cleaning process. We observe I/Pb ratios of 2.87 for SQDs and 3.29 for SQDs-H, the Energy Dispersive Spectroscopy (EDS) findings can back up these conclusions (**Figure S7** and **Table S1**). However, Br^- and Zn^{2+} do not enter the lattice. This result is also consistent with XPS results (**Figure S8**). The percentage of surface halides is significantly increased after surface cleaning. However, these SQDs-H exhibit extremely poor stability, leading to decomposition after storage for one day (**Figure S9b**). High-energy exposed surfaces after cleaning

would cause aggregation and phase transitions of the QDs[38].

We therefore introduce short-chain ligands (3-PA) to exchange the long ligands which are the initial ligands to be used, such as OA and OAm ligands, for further passivating surface traps and improving stability. Under electron beam irradiation, the SQDs-T still demonstrate a very clear morphology and boundary within the size of 4.4 ± 0.4 nm (**Figure 1h** and **Figure S1d**). In contrast to the SQDs-H, SQDs-T exhibit a similar excitonic peak, a slightly blue-shifted emission peak, the emission peak eventually moves to 635 nm. The FWHM is also significantly narrower, only 31 nm, which is consistent with its more concentrated size distribution. Moreover, the PLQY can increase to 99%, which illustrates a further decrease in defects on the SQDs-T by ligand exchange of 3-PA (**Figure 1i**). In **Figure S9**, comparative images of SQDs, SQDs-H and SQDs-T place in the air for one month. Furthermore, SQDs-T exhibit an I/Pb ratio of 3.44. Based on these results, 3-PA has the capacity to successfully attach to exposed areas on SQDs-H surfaces, hence reducing surface imperfections and enhancing the stability of QDs. We observe the lattice spacing of the QDs by using HRTEM. All of them are 0.628 nm (**Figure S2b, c, d**). Thus, affirming that the meticulous surface-cleansing techniques and ligand exchange processes do not disrupt the inherent crystalline arrangement (**Figure S10**). And there are no noticeable peak shifts in the XRD pattern of SQDs-H and SQDs-T compared with that of SQDs, verifying that there is no incorporation of Br^- during the surface-cleaning process.

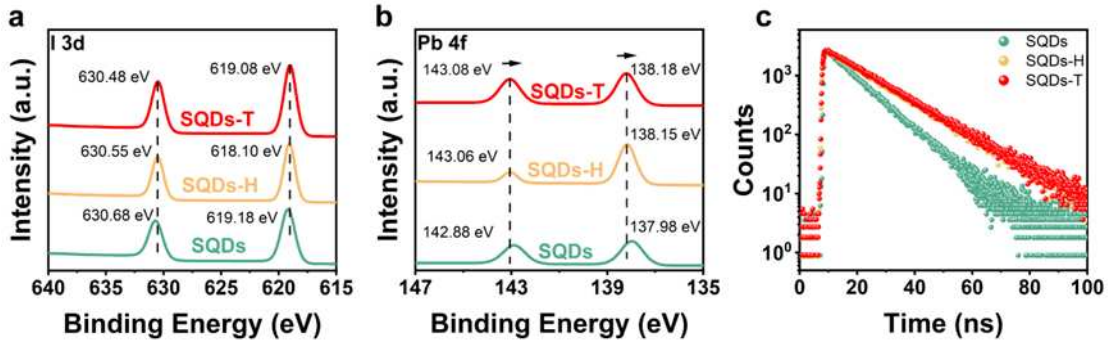

Figure 2. Surface environment of the $CsPbI_3$ QDs. X-ray photoelectron spectroscopy (XPS) spectra for SQDs, SQDs-H and SQDs-T about (a) Pb 4f, (b) I 3d and (c) Time-resolved PL (TRPL) decay spectra of SQDs, SQDs-H and SQDs-T.

To understand the surface coordination environment, we employe XPS. A slow transform towards a low binding energy for I 3d can be observe in SQDs-H and SQDs-T, as compared to the SQDs (**Figure 2a**), which for SQDs-H is attributed to the formation of I^--rich QDs surfaces after surface-cleaning by acid. And the chemical environment surrounding by iodine atoms is changed, leading to a big change in the binding energy measured by XPS. For SQDs-T, this observation can potentially be related to the existence of 3-PA on the surface, which results from the competition between 3-PA and I^- for binding to Pb^{2+}, leading to a difference in the local environment around the iodide ions. In contrast, the SQDs-H and SQDs-T show a step-by-step transition to high binding energies for Pb 4f compared to the SQDs (**Figure 2b**). There are stronger interactions between Pb and I in $[PbI_6]^{4-}$ octahedra. Also, 3-PA on the

surface of the SQDs-T interacts with Pb^{2+} in the form of unprotonated and strongly bound species, effectively passivating the surface iodide vacancies[39].

In order to further elucidate the defect density of QDs, we carry out the TRPL decay spectrum. The detailed conclusions can be observed in **Figure 2c** and **Table S2**[40]. Compared with the dynamics of QDs-M (**Figure S11**), we find that SQDs, SQDs-H and SQDs-T exhibit a nearly single-exponential decay (**Figure 2c**). The PL lifetime of the SQDs-T and SQDs-H are 15.3 and 14.9 ns, separately. Both of them are significantly longer than SQDs (12.6 ns), suggesting much reduced trap-assisted non-radiative channels in the SQDs-H and SQDs-T. These results serve as compelling evidence of the significantly reduced nonradiative rate by surface-cleaning and ligand exchange. Urbach energy of QDs is calculated (**Figure S12**), which is corroborated by the TRPL results. **Figures S13** and **S14** demonstrate the monitoring of the PL peak variations of QDs-M and SQDs-T. In contrast, SQDs-T exhibit excellent UV stability, in which FWHM and the peak of the PL spectrum remain almost unchanged under UV exposure for 180 min. With the time prolongation, the SQDs-T maintain excellent and stable pure-red PL emission at 635 nm.

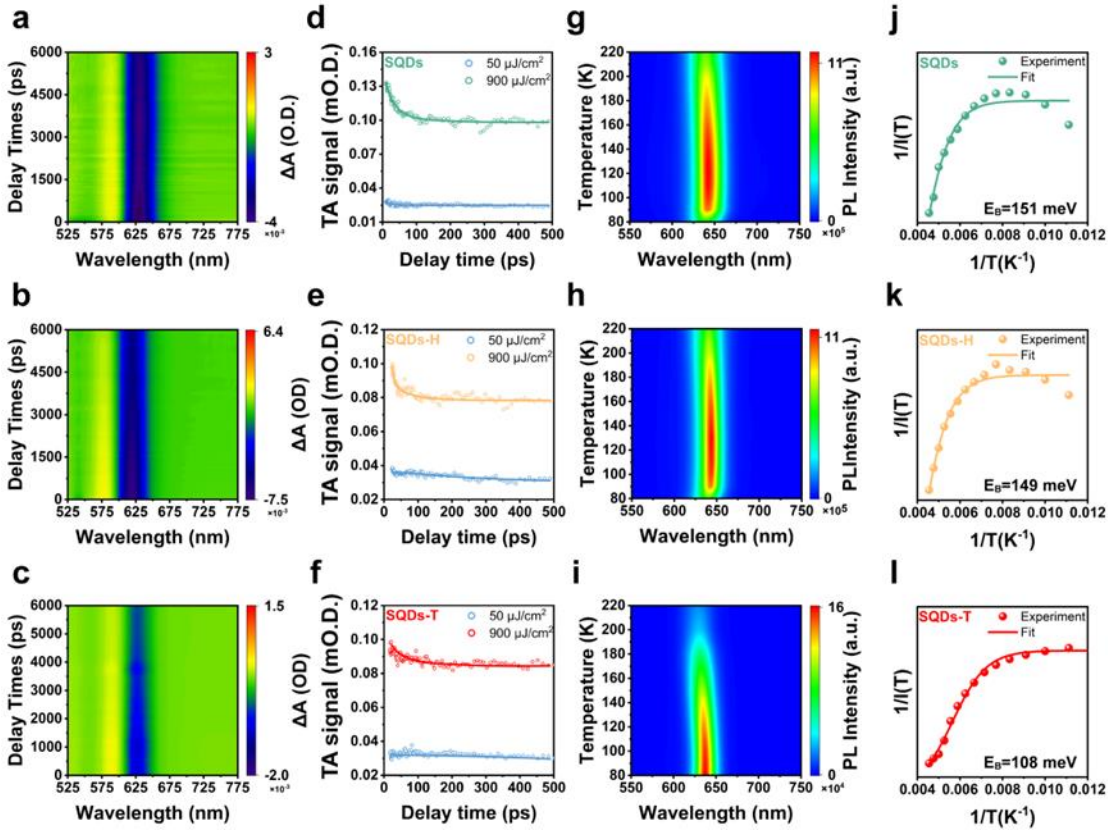

Figure 3. Photoexcited Carrier dynamics of QDs. Pseudo color image of femtosecond transient absorption (TA) spectra of (a) SQDs, (b) SQDs-H, and (c) SQDs-T; TA bleach recovery kinetics of (d) SQDs, (e) SQDs-H, and (f) SQDs-T at different pulse energy density; Temperature-dependent spectra of (g) SQDs, (h) SQDs-H, and (i) SQDs-T; Integrated PL intensity for (j) SQDs, (k) SQDs-H, and (l) SQDs-T about the reciprocal temperature ranging from 80 to 220 K.

TA measurements are conducted to corroborate the exceptional optical performance of SQDs-T. Using a 420 nm femtosecond laser as the pump source, the SQDs show a negative probe bleaching at 631 nm (**Figure 3a**). Meanwhile, the

bleaching signals of SQDs-H and SQDs-T are observed at 627 nm (**Figure 3b, c**), which is similar to the absorption peak in the UV spectra. Ground-state bleaching (GSB) occurs when the absorption of photons reduces the population of the ground electronic state[41]. In general, there is serious Auger recombination in strongly-confined QDs[42,43]. Subsequently, we delve into the exploration of various dynamic processes within QDs through the manipulation of the pump intensity. It becomes evident from **Figure 3d, e, f** and **Figure S15** that distinct decay processes are observed among SQDs, SQDs-H, and SQDs-T when expose to varying degrees of pump intensity. The accompanying data in the Supplementary Information provides a comprehensive analysis. The fitting curve of SQDs-T displays a slower decline and follows a single-exponential decay trend. The fitting value of SQDs-T is 4061.1 ps under the low pulse energy density of 50 μJ/cm^2. In contrast, the decay times for both SQDs (821.5 ps) and SQDs-H (1678.1 ps) are notably shorter than SQDs-T, indicating a considerably lower density of trapping sites in SQDs-T (**Table S3**). SQDs can be characterized by double-exponential bleach recovery kinetics once the pump power approaches 900 μJ/cm^2 (**Table S4**). This behavior is observed as a fast component with a duration of 23.1 ps (τ_1, 13.2%) and a long component lasting 1181.9 ps (τ_2, 86.8%). The fast component (τ_1) can be ascribed to trap-assisted Auger recombination. And the longer component (τ_2) arises from intrinsic edge exciton recombination[44]. SQDs-H show a slower decay rate than the SQDs under the same pump intensity with a fast component of 15.1 ps (τ_1, 4.8%) and a long component of 1223.5 ps (τ_2, 94.2%), which indicates that the removal of defects during the surface cleaning can suppress trap-assisted Auger recombination. The bleach recovery dynamics of SQDs-T show a nearly single exponential characterized by two constants: 58.1 ps (τ_1, 1.01%) and 2235.5 ps (τ_2, 98.9%). And we calculate the biexciton lifetime of three QDs (**Figure S16**). SQDs-T show a much longer-biexciton lifetime (74.9 ps) compared with SQDs (37.6 ps) and SQDs-H (23.0 ps), indicating that Auger recombination inside SQDs-T is significantly inhibited.

Too high exciton binding energy (E_B) of strongly confined QDs can also cause the Auger recombination process[45]. A temperature dependence of PL measurements is used to calculate the E_B of QDs (**Figure 3g, h, i**), where we estimate the E_B of QDs based on the function between *I(T)* and *T* from 80 to 220 K. SQDs-T show a much lower E_B (108 meV) than the SQDs (151 meV) and SQDs-H (149 meV) (**Figure 3j, k, l**). We consider that the introduction of 3-PA not only removes defects, but also can change the superficial charge distribution of SQDs-T as an electron acceptor, affecting the interaction between carriers and excitons, and resulting in a decrease of E_B. It appears that the diminished Auger recombination is also an outcome of the low E_B which is observed in this study. This observation result is consistent with the theoretical basis. Additionally, the mechanism of the suppressed Auger recombination has been clarified by first-principles calculations based on the DFT. Based on this analysis, we can see how 3-PA affects the charge distribution on QD surfaces to inhibit trap-assisted nonradiative recombination and Auger recombination. This is further elucidated and discussed in **Figures S17-S19**. The results acquire from the DFT computations and the temperature-dependent PL spectra provide clear evidence.

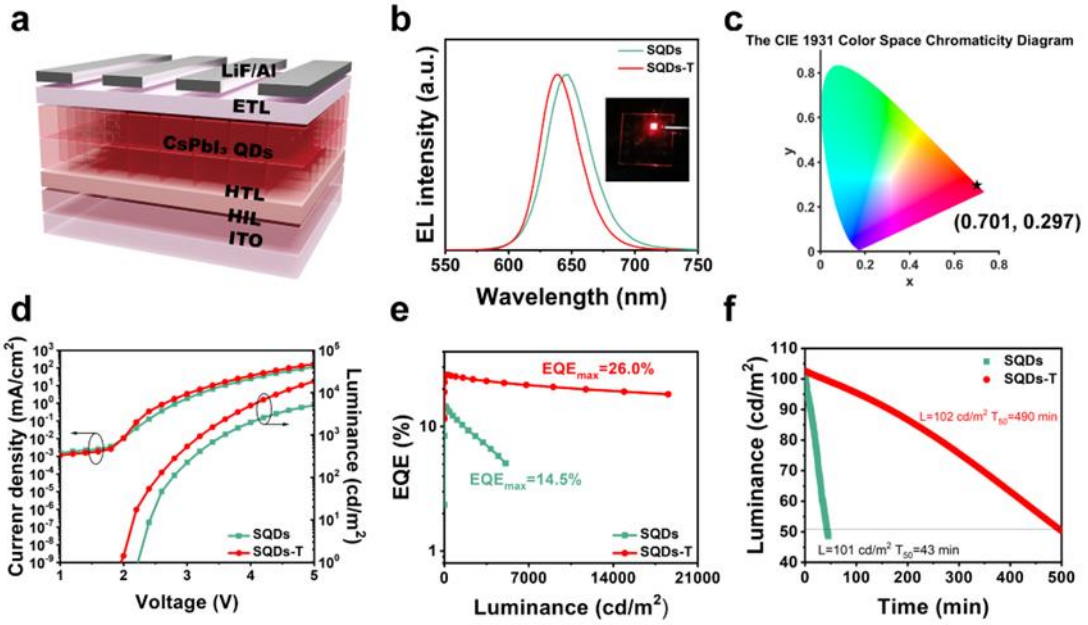

Figure 4. A comparison of the performance of PeLEDs. (a) Illustration showing the structural layout of the LED; (b) EL spectrum of PeLEDs employed SQDs and SQDs-T, the inset displays an image of the PeLEDs employed SQDs-T working at 3.5 V; (c) PeLED coordinates according to CIE; Curves for (d) Current density-voltage-luminance (J-V-L) and (e) EQE-L for PeLEDs used SQDs and SQDs-T; (f) T_{50} is calculated for PeLEDs using SQDs and SQDs-T, with an original luminance of 101 cd m^{-2} and 102 cd m^{-2}, respectively.

We have fabricated PeLEDs using these QDs (**Figure 4a**). Due to the serious phase separation of QDs-M and poor stability of SQDs-H, there are no EL properties of PeLEDs based on these two QDs. **Figure S20** shows a schematic diagram of the LED valence band edge of SQDs and SQDs-T, in which the hole injection barrier shows a significant decrease from 0.12 to 0.09 eV with the help of 3-PA. The PeLEDs, which are based on SQDs-T, exhibit a perfectly symmetric pure-red EL peak at a wavelength of 638 nm. The FWHM is only 32 nm (**Figure 4b**). This can be understood in terms of the CIE coordinates, specifically denoted as (0.701, 0.297) as presented in **Figure 4c**. The coordinate of PeLEDs based on SQDs-T is very close to the National Television System Committee (NTSC) standard. The SQDs-T devices exhibit a slightly narrower FWHM than that of PeLEDs based on SQDs, which is associated with the better distribution of SQDs-T sizes. The J-V-L curves of the PeLEDs are displayed in **Figure 4d**. PeLEDs based on SQDs-T exhibit a lower activation voltage of 2.0 V, but SQDs devices require 2.3 V. In addition, the PeLEDs based on SQDs-T demonstrate lower leak current and higher maximum luminance (18500 cd/m^2) at the same voltage than those of SQDs PeLEDs (5060 cd/m^2). PeLEDs based on SQDs-T exhibit a peak EQE of 26.0%, much higher than that of SQDs PeLEDs with a low EQE of 14.5% (**Figure 4e**). The average peak EQE (counting 50 devices) of PeLEDs with SQDs-T (22.0%) manifest good reproducibility of the device performances (**Figure S21**). We find that PeLEDs based on SQDs-T achieve the maximum EQE at a higher luminance (280.8 cd/m^2) than PeLEDs based on SQDs (8.7 cd/m^2). This difference is likely attributed to the inhibition of Auger recombination within SQDs-T. And the PeLEDs employing SQDs-T exhibit significantly reduced efficiency roll-off as opposed to the SQDs at high

luminance conditions. With a 10000 cd/m^2 device luminance, the EQE of the SQDs-T PeLEDs drops to 21.0%. However, the EQE of SQD PeLEDs drops to only 5.0% when the luminance is increased to 5000 cd/m^2. These results indicate that SQDs-T PeLEDs achieve high EQE at high brightness, which is important for display applications. SQDs-T PeLEDs exhibit a high EQE at high luminance, which is crucial for monitor applications. It suggests that SQDs-T PeLEDs have less Auger recombination, leading to improved performance.

There is an essential requirement for PeLEDs to have stable spectral and operational characteristics in order to be used for various applications. In order to assess the stability of these devices, a strict test is conducted using a constant current density (**Figure S22**). The luminance of the initial luminance is 102 cd/m^2, and the operational T_{50} of the SQDs-T device is 490 min (**Figure 4f**). Notably, the SQDs-T based device has a negligible change in the emission wavelength and shape of the EL spectra (**Figure S23**). SQDs-T device has a life expectancy nearly 11 times longer than SQDs-based device (T_{50} = 43 min, the original luminance is 101 cd/m^2). Furthermore, the hysteresis of LED based SQDs and SQDs-T have been examined by measuring the J-V curves in various scanning orientations (**Figure S24**). Compared to the reported advanced pure-red QD PeLEDs published in the literature, our device exhibits a comprehensive set of excellent properties (EQE, luminance, spectral and operational stability) (**Table S5**).

In this work, a novel strategy for obtaining $CsPbI_3$ QDs with strong confinement and suppressed nonradiative recombination has been developed. Firstly, we construct the iodide-rich environment to synthesize pure-red single-halide $CsPbI_3$ QDs (size only ~ 5 nm), achieving a small size with a narrow distribution. Subsequently, we propose a surface cleaning and ligand exchange to remove wastes from the QDs surface. Additionally, the ligand exchange between 3-PA and long-chain ligands will further improve the electrical properties of QDs. The resulting QDs achieve pure-red emission at 635 nm. It is noteworthy that the FWHM is only 31 nm, and the PLQY is 99%. DFT simulations confirm that the 3-PA effectively stores electrons and reduces the build-up of charge in QDs. Auger recombination in QDs can be suppressed by reduced E_B and trap-assisted Auger recombination process. Finally, we made additional advancements in the development of PeLEDs devices that exhibit spectrum stability and generate a pure red light. These devices have an EL peak at 638 nm. The max luminance is 18500 cd/m^2, and the maximum EQE is 26.0%. Moreover, the PeLEDs exhibit a suppressed efficiency roll-off. And the PeLEDs also demonstrate a remarkable stability of the EL spectrum by its persistent absence of serious shifts, even when expose to high working voltages. The PeLEDs show excellent operational stability with a long T_{50} (490 min) and the original luminance is 102 cd/m^2, which represents one of the most advanced pure-red LEDs nowadays.

Supporting Information

The Supporting Information is available free of charge by the author.

Additional experimental details, materials, and methods, including characterization, device fabrication, computational method in Experimental Section. Calculation of Urbach energy, exciton binding energy and EQE of PeLEDs in Supplementary Notes. The size distribution histograms of

QDs-M, SQDs, SQDs-H and SQDs-T (Figure S1); the HAADF-STEM images, simulated crystal structures and FFT patterns of QDs-M, SQDs, SQDs-H and SQDs-T (Figure S2); the absorption spectra of Pb-precursor solutions (Figure S3); in-situ PL spectra of QDs-M and SQDs (Figure S4); the optical properties and morphological characteristics of QDs produced by different quenching speeds (Figure S5); the PL and UV-vis spectra of SQDs with different adding order of HBr (Figure S6); EDS images of QDs-M, SQDs, SQDs-H and SQDs-T (Figure S7); XPS spectra of SQDs and SQDs-T (Figure S8); the photographs of SQDs, SQDs-H and SQDs-T preserved in a room temperature environment (Figure S9); XRD of QDs-M, SQDs, SQDs-H and SQDs-T (Figure S10); TRPL spectra of QDs-M (Figure S11); Urbach energies of QDs-M, SQDs, SQDs-H and SQDs-T (Figure S12); evolution of PL spectra of QDs-M and SQDs-T under prolonged UV irradiation (Figure S13); evolution of PL spectra of QDs-M and SQDs-T under prolonged storage in a room temperature environment (Figure S14); power dependent kinetic traces of SQDs, SQDs-H and SQDs-T at the exciton bleach (Figure S15); biexciton recombination kinetics of SQDs, SQDs-H and SQDs-T (Figure S16); DFT results of the adsorption structures and energies of OA, OAm and 3-PA binding to the surface of QDs (Figure S17); the DOS for QDs (Figure S18); the electronic charge density of QDs (Figure S19); the energy level of SQDs and SQDs-T (Figure S20); histograms of EQE of PeLEDs based on SQDs and SQDs-T (Figure S21); EL spectra of devices at different operational voltages (Figure S22); evolutions of EL spectra during the measurement of operational half-lifetime T50 (Figure S23); the investigation of hysteresis in SQDs-based LED and SQDs-T-based LED (Figure S24); the concentration of different elements in QDs-M, SQDs, SQDs-H and SQDs-T from EDS mapping (Table S1); TRPL fitting parameters of QDs-M, SQDs, SQDs-H and SQDs-T (Table S2); TA spectra fitting parameters of QDs-M, SQDs, SQDs-H and SQDs-T under the low pulse energy density (Table S3); TA spectra fitting parameters of QDs-M, SQDs, SQDs-H and SQDs-T under the high pulse energy density (Table S4); the performance of a typical PeLEDs device with pure-red emission (Table S5).

Author contributions

†K.R., J.C.H. and C.H.B. made equal contributions, so they should be acknowledged as co-first authors. K.R. and C.H.B. started and designed the study. S.B.W., K.R. and J.C.H. performed experiments and analyzed data. C.H.B. and K.R. performed PeLEDs devices and tested them. N.H.d.L. and X.Y.W. conducted and analyzed the theoretical calculations. S.B.W., K.R. and W.X.W. made the optical measurements and analyzed data. J.C.H., Y.L. and M.L.S took the TEM images and analyzed them. C.H.B., Y.L., M.L.S. and W.X.W. guided the projects. C.H.B., Y.L., M.L.S. and W.X.W. revised the paper.

Notes

The authors declare no conflict of interest.

Associated Content

Acknowledgments

We gratefully acknowledge all of the funds which support this work. This work is financially supported by the National Natural Science Foundation of China (No. 52302171, 12074016 and

12274009), Shandong Provincial Natural Science Foundation, China (ZR2023QF005), Heilongjiang Provincial Natural Science Foundation of China (LH2023F026, LH2020A007 and LH2020F027), New Era Longjiang Excellent Doctoral Dissertation Project (LJYXL2022-003), the Research and Development Project from the Shanxi-Zheda Institute of Advanced Materials and Chemical Engineering (2022SX-TD001), Teaching Reform Research Project of Harbin Engineering University (79005023/013) and the Fundamental Research Funds for the Central Universities (3072024XX2606, 3072022TS2613, 79000012/012).

References

(1) Ma, D.; Lin, K.; Dong, Y.; Choubisa, H.; Proppe, A. H.; Wu, D.; Wang, Y.-K.; Chen, B.; Li, P.; Fan, J. Z.; Yuan, F.; Johnston, A.; Liu, Y.; Kang, Y.; Lu, Z.-H.; Wei, Z.; Sargent, E. H. Distribution Control Enables Efficient Reduced-Dimensional Perovskite LEDs. *Nature* **2021**, *599*, 594–598.

(2) Lin, K.; Xing, J.; Quan, L. N.; de Arquer, F. P. G.; Gong, X.; Lu, J.; Xie, L.; Zhao, W.; Zhang, D.; Yan, C.; Li, W.; Liu, X.; Lu, Y.; Kirman, J.; Sargent, E. H.; Xiong, Q.; Wei, Z. Perovskite Light-Emitting Diodes with External Quantum Efficiency Exceeding 20 per Cent. *Nature* **2018**, *562*, 245–248.

(3) Liu, X.-K.; Xu, W.; Bai, S.; Jin, Y.; Wang, J.; Friend, R. H.; Gao, F. Metal Halide Perovskites for Light-Emitting Diodes. *Nat. Mater.* **2021**, *20*, 10–21.

(4) Kovalenko, M. V.; Protesescu, L.; Bodnarchuk, M. I. Properties and Potential Optoelectronic Applications of Lead Halide Perovskite Nanocrystals. *Science* **2017**, *358* (6364), 745–750.

(5) Dong, H.; Ran, C.; Gao, W.; Li, M.; Xia, Y.; Huang, W. Metal Halide Perovskite for Next-Generation Optoelectronics: Progresses and Prospects. *eLight* **2023**, *3*, 3.

(6) Shan, Q.; Wei, C.; Jiang, Y.; Song, J.; Zou, Y.; Xu, L.; Fang, T.; Wang, T.; Dong, Y.; Liu, J.; Han, B.; Zhang, F.; Chen, J.; Wang, Y.; Zeng, H. Perovskite Light-Emitting/Detecting Bifunctional Fibres for Wearable LiFi Communication. *Light Sci. Appl.* **2020**, *9*, 163.

(7) Swarnkar, A.; Marshall, A. R.; Sanehira, E. M.; Chernomordik, B. D.; Moore, D. T.; Christians, J. A.; Chakrabarti, T.; Luther, J. M. Quantum Dot–Induced Phase Stabilization of α-$CsPbI_3$ Perovskite for High-Efficiency Photovoltaics. *Science* **2016**, *354*, 92–95.

(8) Bi, C.; Hu, J.; Yao, Z.; Lu, Y.; Binks, D.; Sui, M.; Tian, J. Self-Assembled Perovskite Nanowire Clusters for High Luminance Red Light-Emitting Diodes. *Adv. Funct. Mater.* **2020**, *30*, 2005990.

(9) Song, J.; Li, J.; Li, X.; Xu, L.; Dong, Y.; Zeng, H. Quantum Dot Light-Emitting Diodes Based on Inorganic Perovskite Cesium Lead Halides ($CsPbX_3$). *Adv. Mater.* **2015**, *27*, 7162–7167.

(10) Huang, H.; Bodnarchuk, M. I.; Kershaw, S. V.; Kovalenko, M. V.; Rogach, A. L. Lead Halide Perovskite Nanocrystals in the Research Spotlight: Stability and Defect Tolerance. *ACS Energy Lett.* **2017**, *2*, 2071–2083.

(11) Bi, C.; Yao, Z.; Sun, X.; Wei, X.; Wang, J.; Tian, J. Perovskite Quantum Dots with Ultralow Trap Density by Acid Etching-Driven Ligand Exchange for High Luminance and Stable Pure-Blue Light-Emitting Diodes. *Adv. Mater.* **2021**, *33*, 2006722.

(12) Hassan, Y.; Park, J. H.; Crawford, M. L.; Sadhanala, A.; Lee, J.; Sadighian, J. C.; Mosconi, E.; Shivanna, R.; Radicchi, E.; Jeong, M.; Yang, C.; Choi, H.; Park, S. H.; Song, M. H.; De Angelis,

F.; Wong, C. Y.; Friend, R. H.; Lee, B. R.; Snaith, H. J. Ligand-Engineered Bandgap Stability in Mixed-Halide Perovskite LEDs. *Nature* **2021**, *591*, 72–77.

(13) Dong, Y.; Wang, Y.-K.; Yuan, F.; Johnston, A.; Liu, Y.; Ma, D.; Choi, M. J.; Chen, B.; Chekini, M.; Baek, S. W.; Sagar, L. K.; Fan, J.; Hou, Y.; Wu, M.; Lee, S.; Sun, B.; Hoogland, S.; Quintero-Bermudez, R.; Ebe, H.; Todorovic, P.; Dinic, F.; Li, P.; Kung, H. T.; Saidaminov, M. I.; Kumacheva, E.; Spiecker, E.; Liao, L. S.; Voznyy, O.; Lu, Z. H.; Sargent, E. H. Bipolar-Shell Resurfacing for Blue LEDs Based on Strongly Confined Perovskite Quantum Dots. *Nat. Nanotechnol.* **2020**, *15*, 668–674.

(14) Bi, C.; Wang, S.; Kershaw, S. V.; Zheng, K.; Pullerits, T.; Gaponenko, S.; Tian, J.; Rogach, A. L. Spontaneous Self-Assembly of Cesium Lead Halide Perovskite Nanoplatelets into Cuboid Crystals with High Intensity Blue Emission. *Adv. Sci.* **2019**, *6*, 1900462.

(15) Chiba, T.; Hayashi, Y.; Ebe, H.; Hoshi, K.; Sato, J.; Sato, S.; Pu, Y. J.; Ohisa, S.; Kido, J. Anion-Exchange Red Perovskite Quantum Dots with Ammonium Iodine Salts for Highly Efficient Light-Emitting Devices. *Nat. Photon.* **2018**, *12*, 681–687.

(16) Zhao, M.; Zhang, Q.; Xia, Z. Narrow-Band Emitters in LED Backlights for Liquid-Crystal Displays. *Mate. Today* **2020**, *40*, 246–265.

(17) Yang, X.; Ma, L.; Yu, M.; Chen, H. H.; Ji, Y.; Hu, A.; Zhong, Q.; Jia, X.; Wang, Y.; Zhang, Y.; Zhu, R.; Wang, X.; Lu, C. Focus on Perovskite Emitters in Blue Light-Emitting Diodes. *Light Sci. Appl.* **2023**, *12*, 177.

(18) Protesescu, L.; Yakunin, S.; Bodnarchuk, M. I.; Krieg, F.; Caputo, R.; Hendon, C. H.; Yang, R. X.; Walsh, A.; Kovalenko, M. V. Nanocrystals of Cesium Lead Halide Perovskites ($CsPbX_3$, X = Cl, Br, and I): Novel Optoelectronic Materials Showing Bright Emission with Wide Color Gamut. *Nano Lett.* **2015**, *15*, 3692–3696.

(19) Dong, W.; Li, H.; Li, J.; Hua, Y.; Yang, F.; Dong, Q.; Zhang, X.; Zheng, W. Precursor Engineering Induced High-Efficiency Electroluminescence of Quasi-Two-Dimensional Perovskites: A Synergistic Defect Inhibition and Passivation Approach. *Nano Lett.* **2024**, 24, 3952–3960.

(20) Guo, J.; Fu, Y.; Zheng, W.; Xie, M.; Huang, Y.; Miao, Z.; Han, C.; Yin, W.; Zhang, J.; Yang, X.; Tian, J.; Zhang, X. Entropy-Driven Strongly Confined Low-Toxicity Pure-Red Perovskite Quantum Dots for Spectrally Stable Light-Emitting Diodes. *Nano Lett.* **2024**, 24, 417–423.

(21) Zhou, W.; Shen, Y.; Cao, L.-X.; Lu, Y.; Tang, Y.-Y.; Zhang, K.; Ren, H.; Xie, F.-M.; Li, Y.-Q.; Tang, J.-X. Manipulating Ionic Behavior with Bifunctional Additives for Efficient Sky-Blue Perovskite Light-Emitting Diodes. *Adv. Funct. Mater.* **2023**, 33, 2301425.

(22) Kim, J. S.; Heo, J. M.; Park, G. S.; Woo, S. J.; Cho, C.; Yun, H. J.; Kim, D. H.; Park, J.; Lee, S. C.; Park, S. H.; Yoon, E.; Greenham, N. C.; Lee, T. W. Ultra-Bright, Efficient and Stable Perovskite Light-Emitting Diodes. *Nature* **2022**, *611*, 688–694.

(23) Yang, J. N.; Song, Y.; Yao, J. S.; Wang, K. H.; Wang, J. J.; Zhu, B. S.; Yao, M. M.; Rahman, S. U.; Lan, Y. F.; Fan, F. J.; Yao, H. B. Potassium Bromide Surface Passivation on $CsPbI_{3-x}Br_x$ Nanocrystals for Efficient and Stable Pure Red Perovskite Light-Emitting Diodes. *J. Am. Chem. Soc.* **2020**, *142*, 2956–2967.

(24) Zhou, Y.; Fang, T.; Liu, G.; Xiang, H.; Yang, L.; Li, Y.; Wang, R.; Yan, D.; Dong, Y.; Cai, B.; Zeng, H. Perovskite Anion Exchange: A Microdynamics Model and a Polar Adsorption Strategy for Precise Control of Luminescence Color. *Adv. Funct. Mater.* **2021**, *31*, 2106871.

(25) Karlsson, M.; Yi, Z.; Reichert, S.; Luo, X.; Lin, W.; Zhang, Z.; Bao, C.; Zhang, R.; Bai, S.; Zheng, G.; Teng, P.; Duan, L.; Lu, Y.; Zheng, K.; Pullerits, T.; Deibel, C.; Xu, W.; Friend, R.; Gao, F. Mixed Halide Perovskites for Spectrally Stable and High-Efficiency Blue Light-Emitting Diodes. *Nat. Commun.* **2021**, *12*, 361.

(26) Xie, M.; Guo, J.; Zhang, X.; Bi, C.; Sun, X.; Li, H.; Zhang, L.; Binks, D.; Li, G.; Zheng, W.; Tian, J. Suppressing Ion Migration of Mixed-Halide Perovskite Quantum Dots for High Efficiency Pure-Red Light-Emitting Diodes. *Adv. Funct. Mater.* **2023**, *33*, 2300116.

(27) Xie, M.; Tian, J. Operational Stability Issues and Challenges in Metal Halide Perovskite Light-Emitting Diodes. *J. Phys. Chem. Lett.* **2022**, *13*, 1962–1971.

(28) Liu, Y.; Dong, Y.; Zhu, T.; Ma, D.; Proppe, A.; Chen, B.; Zheng, C.; Hou, Y.; Lee, S.; Sun, B.; Jung, E. H.; Yuan, F.; Wang, Y.; Sagar, L. K.; Hoogland, S.; García de Arquer, F. P.; Choi, M. J.; Singh, K.; Kelley, S. O.; Voznyy, O.; Lu, Z. H.; Sargent, E. H. Bright and Stable Light-Emitting Diodes Based on Perovskite Quantum Dots in Perovskite Matrix. *J. Am. Chem. Soc.* **2021**, *143*, 15606–15615.

(29) Wang, Y. K.; Yuan, F.; Dong, Y.; Li, J. Y.; Johnston, A.; Chen, B.; Saidaminov, M. I.; Zhou, C.; Zheng, X.; Hou, Y.; Bertens, K.; Ebe, H.; Ma, D.; Deng, Z.; Yuan, S.; Chen, R.; Sagar, L. K.; Liu, J.; Fan, J.; Li, P.; Li, X.; Gao, Y.; Fung, M. K.; Lu, Z. H.; Bakr, O. M.; Liao, L. S.; Sargent, E. H. All-Inorganic Quantum-Dot LEDs Based on a Phase-Stabilized α-$CsPbI_3$ Perovskite. *Angew. Chem. Int. Ed.* **2021**, *60*, 16164–16170.

(30) Lan, Y. F.; Yao, J. S.; Yang, J. N.; Song, Y. H.; Ru, X. C.; Zhang, Q.; Feng, L. Z.; Chen, T.; Song, K. H.; Yao, H. B. Spectrally Stable and Efficient Pure Red $CsPbI_3$ Quantum Dot Light-Emitting Diodes Enabled by Sequential Ligand Post-Treatment Strategy. *Nano Lett.* **2021**, *21*, 8756–8763.

(31) Ding, S.; Hao, M.; Lin, T.; Bai, Y.; Wang, L. Ligand Engineering of Perovskite Quantum Dots for Efficient and Stable Solar Cells. *J. Energy Chem.* **2022**, *69*, 626–648.

(32) Yumoto, G.; Tahara, H.; Kawawaki, T.; Saruyama, M.; Sato, R.; Teranishi, T.; Kanemitsu, Y. Hot Biexciton Effect on Optical Gain in $CsPbI_3$ Perovskite Nanocrystals. *J. Phys. Chem. Lett.* **2018**, *9*, 2222–2228.

(33) Xue, J.; Wang, R.; Yang, Y. The Surface of Halide Perovskites from Nano to Bulk. *Nat. Rev. Mater.* **2020**, *5*, 809–827.

(34) Yao, J. S.; Ge, J.; Wang, K. H.; Zhang, G.; Zhu, B. S.; Chen, C.; Zhang, Q.; Luo, Y.; Yu, S. H.; Yao, H. B. Few-Nanometer-Sized α-$CsPbI_3$ Quantum Dots Enabled by Strontium Substitution and Iodide Passivation for Efficient Red-Light Emitting Diodes. *J. Am. Chem. Soc.* **2019**, *141*, 2069–2079.

(35) Meggiolaro, D.; Mosconi, E.; De Angelis, F. Formation of Surface Defects Dominates Ion Migration in Lead-Halide Perovskites. *ACS Energy Lett.* **2019**, *4*, 779–785.

(36) Dong, Y.; Qiao, T.; Kim, D.; Parobek, D.; Rossi, D.; Son, D. H. Precise Control of Quantum Confinement in Cesium Lead Halide Perovskite Quantum Dots via Thermodynamic Equilibrium. *Nano Lett.* **2018**, *18*, 3716–3722.

(37) Stamplecoskie, K. G.; Manser, J. S.; Kamat, P. V. Dual Nature of the Excited State in Organic–Inorganic Lead Halide Perovskites. *Energy Environ. Sci.* **2014**, *8*, 208–215.

(38) Hu, J.; Bi, C.; Zhang, X.; Tian, B.; Lu, Y.; Tian, J.; Sui, M. Origin of the Bias Instability in $CsPbI_3$ Light-Emitting Diodes. *Appl. Surf. Sci.* **2023**, *626*, 157289.

(39) Xie, M.; Guo, J.; Zhang, X.; Bi, C.; Zhang, L.; Chu, Z.; Zheng, W.; You, J.; Tian, J. High-Efficiency Pure-Red Perovskite Quantum-Dot Light-Emitting Diodes. *Nano Lett.* **2022**, 22, 8266–8273.

(40) Xu, L.; Liu, G.; Xiang, H.; Wang, R.; Shan, Q.; Yuan, S.; Cai, B.; Li, Z.; Li, W.; Zhang, S.; Zeng, H. Charge-Carrier Dynamics and Regulation Strategies in Perovskite Light-Emitting Diodes: From Materials to Devices. *Appl. Phys. Rev.* **2022**, *9*, 021308.

(41) Liu, Q.; Wang, Y.; Sui, N.; Wang, Y.; Chi, X.; Wang, Q.; Chen, Y.; Ji, W.; Zou, L.; Zhang, H. Exciton Relaxation Dynamics in Photo-Excited $CsPbI_3$ Perovskite Nanocrystals. *Sci Rep* **2016**, *6*, 29442.

(42) Bi, C.; Yao, Z.; Hu, J.; Wang, X.; Zhang, M.; Tian, S.; Liu, A.; Lu, Y.; de Leeuw, N. H.; Sui, M.; Tian, J. Suppressing Auger Recombination of Perovskite Quantum Dots for Efficient Pure-Blue-Light-Emitting Diodes. *ACS Energy Lett.* **2023**, *8*, 731–739.

(43) Huang, P.; Sun, S.; Lei, H.; Zhang, Y.; Qin, H.; Zhong, H. Nonlocal Interaction Enhanced Biexciton Emission in Large $CsPbBr_3$ Nanocrystals. *eLight* **2023**, *3*, 10.

(44) Quintero-Bermudez, R.; Sabatini, R. P.; Lejay, M.; Voznyy, O.; Sargent, E. H. Small-Band-Offset Perovskite Shells Increase Auger Lifetime in Quantum Dot Solids. *ACS Nano* **2017**, *11*, 12378–12384.

(45) Luo, X.; Lai, R.; Li, Y.; Han, Y.; Liang, G.; Liu, X.; Ding, T.; Wang, J.; Wu, K. Triplet Energy Transfer from $CsPbBr_3$ Nanocrystals Enabled by Quantum Confinement. *J. Am. Chem. Soc.* **2019**, *141*, 4186–4190.